

Accurate Analytic Model of a Parametrically Driven Resonant MEMS Mirror with a Fourier Series Based Torque Approximation

Han Woong Yoo *Member, IEEE*, Stephan Albert, Georg Schitter *Senior Member, IEEE*,

Abstract—An accurate analytic model of a parametrically driven resonant MEMS mirror is proposed using a Fourier series based approximation for out-of-plane comb drive torque. The analytic model consists of slow evolution equations of the amplitude and phase derived by the averaging theorem of perturbation theory. Based on the model, analytic expressions of the primary frequencies and Jacobian are derived, which are computationally efficient and provide additional information on the steady state solutions and local dynamics. Measurement results of frequency response show less than ± 0.04 % in frequency errors from the model for various input voltages, i.e. less than ± 0.8 Hz for the case of a mirror with 2 kHz natural frequency. The eigenfrequency and damping of the Jacobian matrix show a good agreement with measured local dynamics as well. This verifies the high accuracy of the proposed model, which can be used for improvement of the MEMS mirror design parameters and control design for large amplitude operation.

Index Terms—MEMS Mirror, Parametric Resonance, Duffing Equation, Perturbation Theory, Discrete Fourier Transform, Bessel Function, Automotive Lidar

I. INTRODUCTION

MEMS scanning mirrors of the resonant type have received much attention for various applications such as beam steering in automotive lidars thanks to their compactness, robustness, scalability, compatibility for integration in electronic systems, long life time, and low unit costs in large volume production [1], [2]. Especially for long range lidars, resonant MEMS mirrors are of high interest as a supporting technology for autonomous driving in various harsh driving conditions such as a wide range of temperature, pressure and vibration [3]–[9]. If equipped with electrostatic actuation, MEMS mirrors represent a parametrically driven oscillator because of the explicit dependence of the driving torque on the state variable of the oscillator, i.e. the position. Accurate modeling of such resonant MEMS mirrors is crucial to derive design requirements from application, to evaluate the performance of a given design, and to improve design parameters, operation conditions, and control design for MEMS scanning systems [10]–[15]. Furthermore, the model should properly describe the behavior at large amplitudes, which are operating points for most applications.

This work has been supported in part by the Austrian Research Promotion Agency (FFG) under the scope of the LiDcAR project (FFG project number 860819). Han Woong Yoo and Georg Schitter are with Automation and Control Institute (ACIN), TU Wien, Gusshausstrasse 27-29, 1040 Vienna, Austria, and Stephan Albert is with Infineon Technologies AG, Am Campeon 1-15, 85579, Neubiberg, Germany. (corresponding author: Han Woong Yoo; phone: +43 1 58801 376518; e-mail: yoo@acin.tuwien.ac.at)

Analytic models of MEMS mirrors with torsional out-of-plane comb drive actuators are mainly used for qualitative analysis, e.g. for finding unstable regions of the parametric resonance. The accuracy of the analysis depends on the approximations of the comb drive torque. A cubic polynomial approximation is most popular for stability analysis at small amplitudes [12], [16], [17] since it directly leads to the renowned Hill's equation and given results of Floquet theory. Pioneering work has investigated the instability regions of the first five parametric resonances for a MEMS oscillator and investigated the effects of cubic nonlinearities [18]–[21]. The derivative of the Gaussian function has been used as an approximation of the comb drive torque for an analysis of rectangular voltage inputs with various duty cycles [10], [11]. A piecewise approximation is proposed for an analysis of stiffness variation by extra comb drives [22]. Rational functions and hyperbolic functions are also used for analytic approximation of the vertical movement of a cantilever or comb drive torque [23]–[25]. However, cubic models are accurate only for small amplitudes [16], [25], piecewise models contain non-analytic points, and the other approximations by Gaussian, rational, and hyperbolic functions usually have limited accuracy to describe the highly nonlinear torque of the out-of-plane comb drives.

For modeling at large amplitudes, brute force ODE simulation is typically used instead to evaluate the MEMS mirror frequency response [11], [14]. Continuation technique [26], [27] is also applied for analysis of the stable and unstable branches [12], [28]. However, such numerical evaluations are typically time-consuming and provide limited analytic information about stationary solutions. A linearized local model at large amplitudes is derived for a phase locked loop (PLL) based on the timing control concept under assumptions of a rectangular input waveform and a specific phase constraint in operation [15]. For other MEMS devices such as gyroscopes, translational motions for a nonlinear harmonic oscillator with longitudinal in-plane comb drives are described by analytic models using perturbation technique [29], [30]. Thanks to a fine approximation of the comb drive force, the analytic models can accurately describe the hardening and softening behavior of the frequency response including large amplitudes. For parametrically driven MEMS mirrors with out-of-plane comb drive actuators, however, there is no analytic model yet that accurately describes the behavior of the mirror over its full operation range [12], especially at the large amplitudes that are routinely reached in applications.

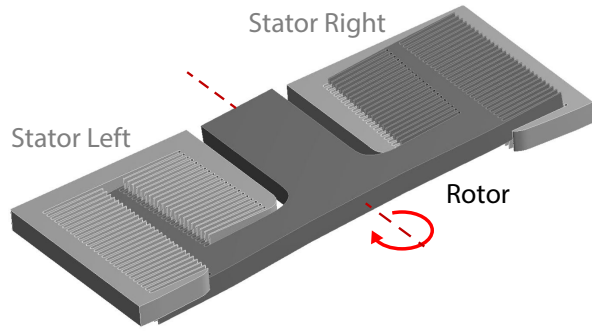


Fig. 1. Perspective view of an out-of-plane electrostatic comb drive for a resonant MEMS mirror. At non-zero deflection angle, an actuation voltage between the stator and the rotor generates a torque acting in the opposite direction, i.e. pulling the drive towards the zero angle state with the maximum capacitance.

The main contribution of this paper is an accurate analytic model of the parametrically driven resonant MEMS mirror for a wide amplitude range. The comb drive torque is approximated by a finite set of analytic functions using discrete Fourier transform (DFT). A frequency domain analysis of the driving torque function is chosen instead of the conventional Taylor expansion in the spatial domain because of the highly nonlinear dependency on angle and because it can be generalized to arbitrarily shaped driving terms. The perturbation technique in [29]–[31] with the Fourier series based torque approximation leads to a slow flow evolution of the amplitude and phase with a series of Bessel functions. This provides an analytic form of the frequency response for the global dynamics and a Jacobian that describes the local dynamics of the MEMS mirror. The analytic solution also allows computationally efficient numerical simulation and permits additional analysis of stationary solutions, e.g. the crossover between the solutions at large amplitudes.

The rest of the paper is organized as follows. First, a single degree of freedom (SDoF) model of the MEMS mirror is described in Section II. Then section III describes an approximation of the comb drive torque by a Fourier series and derives a slow flow model, the analytic solution of the primary frequencies, and the Jacobian matrix. The proposed model is verified by measurement data of the frequency response and the local dynamics in Section IV. Then Section V summarizes the main outcomes of the paper.

II. SDOF MODEL OF RESONANT MEMS MIRROR

Consider a single degree of freedom (SDoF) model for the mechanical deflection angle θ of the resonant MEMS mirror as a generalized Duffing equation [14], [32]

$$I\ddot{\theta} + c(\Theta)\dot{\theta} + k(\theta)\theta = \frac{1}{2} \frac{dC}{d\theta} V^2(t), \quad (1)$$

where I denotes the inertia of the mirror, c is the averaged damping function of the amplitude of the mirror Θ [14], and

k denotes the nonlinear stiffness function defined as

$$c(\Theta) = c_0 + c_1\Theta + c_2\Theta^2 + c_3\Theta^3 + c_4\Theta^4 + c_5\Theta^5, \quad (2)$$

$$k(\theta)\theta = k_1\theta + k_3\theta^3 + k_5\theta^5 + k_7\theta^7, \quad (3)$$

where c_i denotes the nonlinear damping coefficient of the i -th polynomial term of Θ and k_i denotes the nonlinear stiffness coefficient of the i -th polynomial term of θ in (1). The averaged damping function is an approximation of the damping behavior as a function of amplitude that is based on the average energy loss per mirror period, which can be identified by the measured energy loss per period during a passive decay [14], [33]. The constant terms of (2) and (3), i.e. c_0 and k_1 , represent the linear terms of damping and stiffness, e.g. viscous damping and Hooke's spring constant, respectively. The orders of (2) and (3) are chosen as 5 and 7 based on a prior study [14], respectively, to obtain a close fit of the measured data. The specific polynomial orders could also be chosen lower or higher for the purpose of the present analysis without changing the principal insights provided by the following derivations.

The actuation torque is described by the angular derivative of the comb drive capacitance $dC/d\theta$ and the actuation voltage of $V(t)$. For convenience of the analysis, the input voltage is set by a square rooted sine as [16]

$$V(t) = U \sqrt{\frac{1 + \cos \Omega t}{2}}, \quad (4)$$

where U is the peak input voltage and Ω denotes the actuation frequency. Due to the unidirectional pulling torque by out-of-plane comb drive actuators, the resonant MEMS mirror is parametrically excited. This results in oscillations within certain instability regions of the parameter space ($U \times \Omega$). The first order parametric resonance requires twice the mirror frequency for the actuation frequency in steady state [34].

III. ACCURATE ANALYTIC MODEL OF MEMS MIRROR

A. Fourier Series Based Approximation of a Out-of-Plane Comb Drive Torque

For perturbation analysis, the nonlinear dynamics of (1) are desirably analytic for all mirror angles. However, the derivative of the comb drive capacitance is highly nonlinear and varies with the structure of the comb drive. Fig. 1 illustrates a perspective view of an out-of-plane comb drive actuator. The electrode overlap area of the rotor and the stator defines the rough capacitance, which can be described by a piecewise function of the angle in large amplitude operation [22]. Including the fringe effect between the stator and the rotor, the precise capacitance and its angular derivative are highly nonlinear in general and are also dependent on the specific comb drive design.

A Fourier series based approximation is proposed for an accurate model of the angular derivative of the comb drive

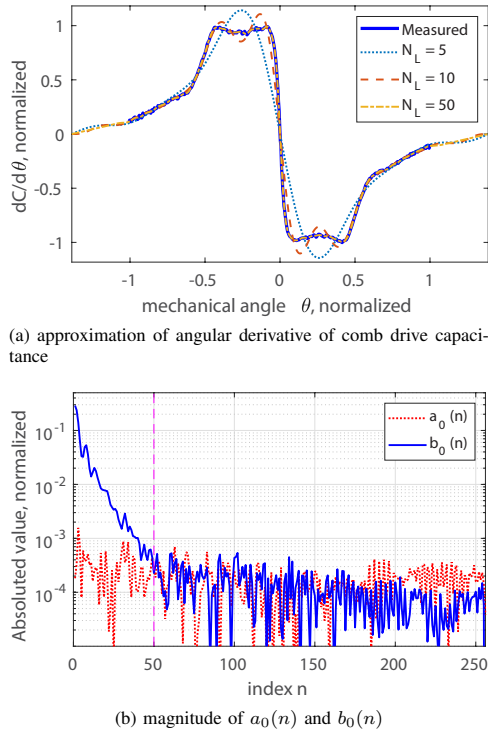


Fig. 2. (a) Measured angular derivative of the comb drive capacitance and its approximation by Fourier series for various N_L . (b) magnitude of Fourier coefficients of $a_0(n)$ and $b_0(n)$ for $N = 512$. The 50th index is indicated by a magenta dashed line for N_L .

capacitance as

$$\frac{dC}{d\theta} = a_0(0) + \sum_{n=1}^{N_L} 2a_0(n) \cos\left(\frac{\pi n \rho_0 \theta}{N}\right) + \sum_{n=1}^{N_L} 2b_0(n) \sin\left(\frac{\pi n \rho_0 \theta}{N}\right), \quad (5)$$

where $a_0(n)$ and $b_0(n)$ denote Fourier coefficients by DFT, which are scaled for convenience of the analysis as

$$a_0(n) = \frac{1}{N} \sum_{l=-N/2}^{N/2-1} \left. \frac{dC}{d\theta} \right|_{\theta=2\rho_0^{-1}l} \cos\left(\frac{2\pi nl}{N}\right), \quad (6)$$

$$b_0(n) = \frac{1}{N} \sum_{l=-N/2}^{N/2-1} \left. \frac{dC}{d\theta} \right|_{\theta=2\rho_0^{-1}l} \sin\left(\frac{2\pi nl}{N}\right), \quad (7)$$

where N denotes the even number for discretization of the comb drive torque, and N_L denotes the finite number of summands for the approximation. The scaling factor of ρ_0 defines a span to the maximum amplitude Θ_{\max} , i.e. $\rho_0 = N/\Theta_{\max}$. The maximum amplitude is chosen to be larger than the range of the scanning angle since (5) defines $dC/d\theta$ as a periodic function of periodicity $2\Theta_{\max}$, i.e. the approximation is not valid for $\theta > \Theta_{\max}$. Essentially, (5) is a representation of a Fourier series based approximation and the DFT in (6) and (7) is a tool to find the Fourier coefficients in (5). In addition,

(5) is defined by even and odd functions via the respective coefficients in (6) and (7). For most resonant mirrors, however, only coefficients $b_0(n)$ of the sine terms can be sufficient since $dC/d\theta$ is typically dominated by odd contributions and vanishes at zero angle [12], [14]. This is a consequence of the typical symmetric design of the comb drive actuator relative to the rotation axis and the use of the same layer in the fabrication process for the stator and the rotor in most devices.

Fig. 2 illustrates a measured angular derivative of the comb capacitance and its approximation with a finite number of Fourier coefficients $b_0(n)$. For a good convergence in a finite N_L , a discontinuity between the positive and negative maximum amplitude can be removed by a constraint, i.e. $\frac{dC(\Theta_{\max})}{d\theta} = \frac{dC(-\Theta_{\max})}{d\theta} = 0$ using linear extrapolation. The magnitude of the coefficients shows that the magnitude of high frequency terms is gradually decreased and reaches a noise floor around $n > 50$. This limited bandwidth can originate from the geometry of the comb drive capacitance or the bandwidth of the sensing circuit. By the Fourier approximation, these noisy high frequency terms are truncated while the major feature of the capacitance derivative is approximated with high accuracy. In addition, the perfect symmetry of $(-\Theta, 0)$ and $(0, \Theta)$ with respect to the origin results in only sine coefficients $b_0(n)$ from (7), and this also limits the number of coefficients for computation. This leads to an analytic representation of the comb drive torque by a finite number of Fourier coefficients.

B. Slow Flow Model of MEMS Mirror

By introducing a dimensionless state variable $x = \theta/\theta_0$, amplitude $A = \Theta/\theta_0$, normalized time $\tau = t/t_0$ where $t_0 = \sqrt{I/k_1}$, which is the inverse of the linear mirror angular frequency $\omega_0 = \sqrt{k_1/I}$, and the normalized actuation frequency $\Omega_a = \Omega t_0$, a dimensionless dynamic equation can be derived from (1), (4) and (5) as

$$\ddot{x} + 2\mu(A)\dot{x} + x + K_3x^3 + K_5x^5 + K_7x^7 = (1 + \cos\Omega_a\tau) \times \left(\frac{1}{2}a(0) + \sum_{n=1}^{N_L} a(n) \cos(\rho nx) + b(n) \sin(\rho nx) \right), \quad (8)$$

where the dimensionless damping and stiffness coefficients and actuation parameters are defined by

$$\mu(A) = \frac{c(A\theta_0)t_0}{2I}, \quad K_3 = \frac{k_3\theta_0^2t_0^2}{I}, \quad K_5 = \frac{k_5\theta_0^4t_0^2}{I}, \quad K_7 = \frac{k_7\theta_0^6t_0^2}{I},$$

$$a(n) = \frac{U^2t_0^2a_0(n)}{2I\theta_0}, \quad b(n) = \frac{U^2t_0^2b_0(n)}{2I\theta_0}, \quad \rho = \frac{\pi\theta_0\rho_0}{N}. \quad (9)$$

Based on perturbation theory [30], [31], (8) can be rewritten as

$$\ddot{x} + \sigma^2x = \epsilon \left[-2\mu(A)\dot{x} + (\sigma^2 - 1)x - K_3x^3 - K_5x^5 - K_7x^7 + (1 + \cos\Omega_a\tau) \left(\frac{1}{2}a(0) + \sum_{n=1}^{N_L} a(n) \cos(\rho nx) + b(n) \sin(\rho nx) \right) \right], \quad (10)$$

where ϵ is a dimensionless parameter, which is used as a bookkeeping device [29], [31], [35] for separating the large terms from the small terms. For weakly nonlinear oscillators, where the damping term is assumed small, it isolates the linear

terms from the nonlinear terms including damping in (8). The value of ϵ scales the nonlinearity and the full nonlinearity is defined by $\epsilon = 1$ [30], [35]. The normalized frequency of the mirror is denoted by σ and equals one half of the actuation frequency in the first order parametric resonance, i.e. $\sigma = \Omega_a/2$. The term of σ on the right hand side corrects the frequency error compared to the linear natural frequency $1/t_0$ on the left hand side [30]. The slow times can be defined by scaling as $T_i = \epsilon^i \tau$, i.e. $T_1 = \epsilon \tau$, and the fast time can be rewritten as $T_0 = \tau$. First order perturbation theory decomposes the solution as $x = x_0 + \epsilon x_1$ for small nonlinear terms. The partial derivative operators are defined as $D_i = \frac{\partial}{\partial T_i}$, i.e. $D_0 = \frac{\partial}{\partial T_0}$ and $D_1 = \frac{\partial}{\partial T_1}$. Only considering terms with ϵ^0 and ϵ^1 , Eq. (10) can be rewritten as

$$D_0^2 x_0 + \sigma^2 x_0 = 0, \quad (11)$$

$$D_0^2 x_1 + \sigma^2 x_1 = \Psi(x_0, \sigma, T_0) - 2D_0 D_1 x_0, \quad (12)$$

where a nonlinear function Ψ is defined as

$$\begin{aligned} \Psi(x_0, \sigma, T_0) = & -2\mu(A)D_0 x_0 + (\sigma^2 - 1)x_0 - K_3 x_0^3 - K_5 x_0^5 \\ & - K_7 x_0^7 + (1 + \cos 2\sigma\tau) \left(\frac{1}{2} a(0) \right. \\ & \left. + \sum_{n=1}^{N_L} a(n) \cos(\rho n x_0) + b(n) \sin(\rho n x_0) \right). \end{aligned}$$

Since (11) is an ordinary undamped harmonic oscillator, the solution can be written as

$$x_0 = A(T_1) \cos \underbrace{(\sigma T_0 + \beta(T_1))}_{\omega}, \quad (13)$$

where $A(T_1)$ and $\beta(T_1)$ denote the dimensionless amplitude and phase in slow time evolution, respectively. The dimensionless amplitude has already been used in the description of the nonlinear damping function. By solvability condition [29]–[31], the solution of (11) and (12) satisfies

$$\int_0^{2\pi} [\Psi(x_0, \sigma, T_0) - 2D_0 D_1 x_0] e^{-i\omega} d\omega = 0. \quad (14)$$

For the calculation of the averaging integrals of the sine terms of the comb drive capacitance in (14), the following identities help.

Lemma 1. *The average of a period for the sine terms of the comb drive torque in (5) is given by*

$$\int_0^{2\pi} \sin(\rho n A \cos \omega) \cos \omega d\omega = 2\pi J_1(\rho n A), \quad (15)$$

$$\int_0^{2\pi} \sin(\rho n A \cos \omega) \sin \omega d\omega = 0, \quad (16)$$

$$\begin{aligned} & \int_0^{2\pi} \sin(\rho n A \cos \omega) \cos \omega \cos(2\omega - 2\beta) d\omega \\ &= 2\pi \left(J_1(\rho n A) - 2 \frac{J_2(\rho n A)}{\rho n A} \right) \cos 2\beta, \end{aligned} \quad (17)$$

$$\begin{aligned} & \int_0^{2\pi} \sin(\rho n A \cos \omega) \sin \omega \cos(2\omega - 2\beta) d\omega \\ &= 2\pi \left(2 \frac{J_2(\rho n A)}{\rho n A} \right) \sin 2\beta, \end{aligned} \quad (18)$$

where $J_\nu(z)$ is the Bessel function of the first kind.

The proof of the lemma is given in Appendix A. Furthermore, the integrals for cosine terms in (5) can be obtained from the following corollary.

Corollary 2. *The average of a period of the cosine terms in the comb drive torque is given by*

$$\int_0^{2\pi} \cos(\rho n A \cos \omega) \cos \omega d\omega = 0, \quad (19)$$

$$\int_0^{2\pi} \cos(\rho n A \cos \omega) \sin \omega d\omega = 0, \quad (20)$$

$$\int_0^{2\pi} \cos(\rho n A \cos \omega) \cos \omega \cos(2\omega - 2\beta) d\omega = 0, \quad (21)$$

$$\int_0^{2\pi} \cos(\rho n A \cos \omega) \sin \omega \cos(2\omega - 2\beta) d\omega = 0. \quad (22)$$

Moreover, the terms related to $a(0)$ vanish in (14) by trigonometric identities. With Corollary 2, this means that even contributions of the capacitance derivative $a(n)$ including $a(0)$ of an asymmetric comb drive would not influence the mirror dynamics for parametrically driven MEMS mirrors. This is due to the fact that the actuation frequency of the first order parametric resonance is twice the mirror frequency. Even torque contributions from $a(n)$ annihilate themselves over a full mirror period and the corresponding net energy injection is zero.

By the lemma and corollary, the slow flow mirror dynamics are obtained by splitting the real and the imaginary part of the integral in (14), each of which has to vanish separately. For positive amplitude, i.e. $A > 0$, the slow flow amplitude and phase evolution of (13) for the dimensionless mirror dynamics (8) are

$$\frac{dA}{dT_1} = -\mu(A)A - \sigma^{-1} \tilde{J}_S(A) \sin(2\beta), \quad (23)$$

$$\begin{aligned} \frac{d\beta}{dT_1} = & \frac{3K_3 A^2}{8\sigma} + \frac{5K_5 A^4}{16\sigma} + \frac{35K_7 A^6}{128\sigma} - \frac{(\sigma^2 - 1)}{2\sigma} \\ & - \sigma^{-1} \left(\tilde{J}_Z(A) + \tilde{J}_C(A) \cos(2\beta) \right), \end{aligned} \quad (24)$$

where the amplitude-dependent sine, constant, and cosine actuation coefficients are defined by

$$\tilde{J}_S(A) = \sum_{n=1}^{N_L} 2b(n) \left(\frac{J_2(\rho n A)}{\rho n A} \right), \quad (25)$$

$$\tilde{J}_Z(A) = \frac{1}{A} \sum_{n=1}^{N_L} b(n) J_1(\rho n A), \quad (26)$$

$$\tilde{J}_C(A) = \frac{1}{A} \sum_{n=1}^{N_L} b(n) \left(\frac{\rho n A J_1(\rho n A) - 2J_2(\rho n A)}{\rho n A} \right), \quad (27)$$

and the primary frequency of equilibrium is

$$\begin{aligned} \sigma = & \left[1 + \frac{3K_3 A^2}{4} + \frac{5K_5 A^4}{8} + \frac{35K_7 A^6}{64} \right. \\ & \left. - 2\tilde{J}_Z(A) \pm 2\tilde{J}_C(A) \sqrt{1 - \left(\frac{-\mu(A)A\sigma}{\tilde{J}_S(A)} \right)^2} \right]^{1/2}. \end{aligned} \quad (28)$$

The detailed derivation is given in Appendix B. The averaged damping is keeping its form during the derivation, indicating that it is a part of the slow flow approximation of various damping effects. The primary frequency can be obtained by an iterative manner for a given amplitude, starting from $\sigma = 1$. The backbone curve, which describes the amplitude-frequency dependence of free oscillations without actuation, is obtained by setting the voltage input to zero, i.e. $\tilde{J}_Z(A) = \tilde{J}_C(A) = \tilde{J}_S(A) = 0$ [32]. The peak amplitude is obtained when σ has an equal root for A , i.e. $|\mu(A)A\sigma| = |\tilde{J}_S(A)|$.

The stability of the equilibrium can be analyzed by the Jacobian matrix at the equilibrium. Assume a solution and its small deviations of ξ and ζ from a steady state as [36]

$$\begin{aligned} A_i(T_1) &= \bar{A}_i + \varepsilon \xi(T_1), \\ \beta_i(T_1) &= \bar{\beta}_i + \varepsilon \zeta(T_1), \end{aligned} \quad (29)$$

where \bar{A}_i and $\bar{\beta}_i$ are the i -th equilibrium of the amplitude and phase at the specific frequency σ , respectively. ε denotes another dimensionless parameter for separating the local dynamics from the operational point. By Taylor approximation, the Jacobian matrix is obtained as

$$\begin{bmatrix} \dot{\xi} \\ \dot{\zeta} \end{bmatrix} = \begin{bmatrix} A_{11} & A_{12} \\ A_{21} & A_{22} \end{bmatrix} \begin{bmatrix} \xi \\ \zeta \end{bmatrix}, \quad (30)$$

where

$$A_{11} = -\frac{d(\mu(\bar{A}_i)\bar{A}_i)}{d\bar{A}_i} + \sigma^{-1} \tilde{J}_{ds}(\bar{A}_i) \sin(2\bar{\beta}_i), \quad (31)$$

$$A_{12} = -2\sigma^{-1} \tilde{J}_s(\bar{A}_i) \cos 2\bar{\beta}_i, \quad (32)$$

$$A_{21} = \frac{3K_3\bar{A}_i}{4\sigma} + \frac{5K_5\bar{A}_i^3}{4\sigma} + \frac{105K_7\bar{A}_i^5}{64\sigma} + \sigma^{-1} \left(\tilde{J}_{dz}(\bar{A}_i) + \tilde{J}_{dc}(\bar{A}_i) \cos(2\bar{\beta}_i) \right), \quad (33)$$

$$A_{22} = 2\sigma^{-1} \tilde{J}_c(\bar{A}_i) \sin(2\bar{\beta}_i), \quad (34)$$

with the amplitude derivative of the sine, constant and cosine actuation coefficients as

$$\tilde{J}_{ds}(\bar{A}_i) = \sum_{n=1}^{N_L} 2b(n) \left(\frac{\rho n \bar{A}_i J_3(\rho n \bar{A}_i) - J_2(\rho n \bar{A}_i)}{\rho n \bar{A}_i^2} \right), \quad (35)$$

$$\tilde{J}_{dz}(\bar{A}_i) = \frac{1}{\bar{A}_i} \sum_{n=1}^{N_L} \rho n b(n) J_2(\rho n \bar{A}_i), \quad (36)$$

$$\tilde{J}_{dc}(\bar{A}_i) = \frac{1}{\bar{A}_i^2} \sum_{n=1}^{N_L} b(n) (\rho n \bar{A}_i J_2(\rho n \bar{A}_i) - 2J_3(\rho n \bar{A}_i)). \quad (37)$$

The Jacobian determines if the solution in (28) is stable or not. In addition, it plays an important role to describe the local dynamics near a stable equilibrium by small external disturbances, e.g. external vibration influence [25], [36]. Therefore, it is important for a control design for stable operation [15].

Compared to the brute force simulation, the proposed analytical model is computationally efficient to calculate the set of solutions by (28). The simulation of the global dynamics by (23) and (24) is much more efficient than that by (1) because high frequency oscillation states are omitted. The Jacobian in (30) also allows faster calculation than the numerical calculation of (23) and (24). The drawback of the proposed analytic model is an approximation error compared to the

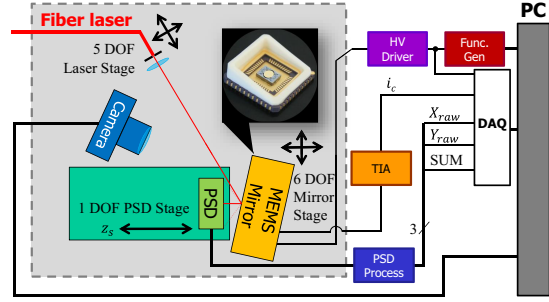


Fig. 3. MEMS test bench and a MEMS mirror for model verification. The mirror and the laser are precisely aligned using a camera and the PSD measurements for varying distance z_s employing a motorized linear stage. The accurate angle conversion from the beam position measurements to the angle is obtained by a dedicated calibration process with the stage while the mirror is operating with a small amplitude. The comb drive capacitance is identified by the transimpedance amplifier that measures the comb drive current.

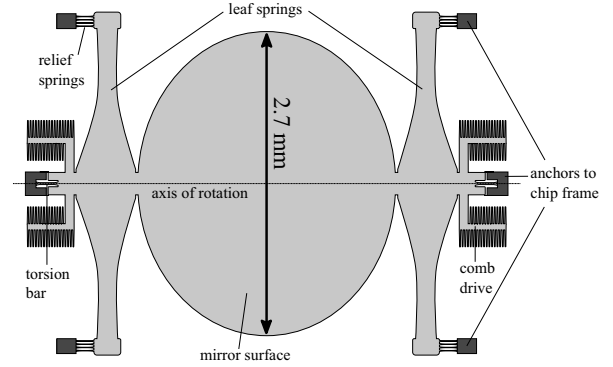


Fig. 4. Conceptual drawing of the MEMS mirror rotor used in the experiments. The mirror surface is elliptical with a long axis of 2.7 mm. The electrostatic drive consists of two pairs of comb drive arms as in Fig. 1. The restoring torque is provided by four leaf spring suspensions and two torsion bars. The leaf springs are connected to the frame via relief springs in order to reduce geometric hardening.

actual mirror behavior. The approximation is mainly due to the perturbation technique of (13), i.e. the steady state solution is a single tone sine while the exact solution is a multitone with harmonics [31]. Therefore the analysis of the harmonic coupling to the other rigid body modes of the scanner is not straightforward. For weakly nonlinear dynamics of MEMS mirrors, the approximation error can be insignificant, allowing a fast and accurate modeling by the proposed method.

IV. MEASUREMENT VERIFICATION

This section describes a verification of the proposed model with measurement data mainly by examining frequency response and local dynamics. Fig. 3 illustrates a MEMS test bench and a MEMS mirror for measurement of the deflection angle [37]. The laser (LPS-660-FC, fiber pigtailed laser, Thorlabs, Newton, NJ, US) shines on the MEMS mirror and then a position sensitive detector (S5991-01, 2D PSD, Hamamatsu, Hamamatsu City, Japan) measures the deflection trajectories of the MEMS mirror via the beam position. The PSD processing

unit provides signals for beam position, which are recorded by a data acquisition card (U2531A, Keysight, Santa Rosa, CA, US). Alignment and calibration schemes using a motorized stage at the PSD allow accurate mirror angle measurements of less than 0.026° accuracy for $\pm 15^\circ$ mechanical mirror angle, whose details are found in [37]. For actuation of the MEMS mirror, the square rooted sine input is generated by a function generator (33522B, Keysight) via a high voltage amplifier (WMA300, Falco systems, Katwijk aan Zee, the Netherlands). The current from the comb drives is measured via a transimpedance amplifier (TIA), used for a comb drive parameter identification and an additional angle sensing of the mirror.

The MEMS mirror used in the experiment is a variant of the MEMS mirror in [14], [15] with an elliptic mirror with a long axis of 2.7 mm. Fig. 4 shows a conceptual drawing of the MEMS mirror with major features. It has two pairs of left and right comb drive arms as in Fig. 1 on both sides of the mirror, each arm having an inner and an outer electrode row for an enhanced torque near zero angle and a compactified design. The MEMS mirror features four leaf spring suspensions extending perpendicularly to the rotation axis and torsional bars at both ends of the rotation axis. The restoring torque for the operational rotational motion is almost entirely ($> 97\%$) provided by the leaf springs and enables high scanning frequencies. The role of the torsion bars is mainly the suppression of other rigid body modes. If directly clamped to the frame, each pair of leaf springs at each side of the mirror would essentially form a doubly clamped beam with excessive geometric hardening. For this reason, the leaf springs are connected to the frame via relief springs for translational flexibility to mitigate the geometric nonlinearities. Further design principles of the leaf spring suspension structures can be inferred from [38]. The mirror also comprises reinforcement structures below the mirror surface to reduce dynamic deformation [39], [40].

The model parameters in (1) can be obtained either by numerical simulation of the MEMS mirror or by experimental identification. From a three-dimensional computer-aided design model of the mirror, the inertia and the stiffness function can be obtained by the finite element method (FEM) and the averaged damping can be retrieved by computational fluid dynamic (CFD) simulations of the air damping [33]. The angular derivative of the comb drive capacitance can be calculated from the angle-dependent geometric overlap of stator and rotor electrodes [22] or FEM simulations of the electrostatic force [28], which additionally account for fringing field effects compared to the geometric overlap. Such an approach combined with the slow-flow model would outline a route towards a fully predictive modeling of the dynamics. However, an individual device will deviate from this nominal behavior due to specification tolerances, e.g. layer thicknesses of raw material, and processing variations. In addition, accurate CFD modeling of the nonlinear damping behavior at large amplitudes is particularly time-consuming and challenging. For these reasons, parameter identification from measurements has been chosen for the present analysis in order to demonstrate the high accuracy of the solutions of

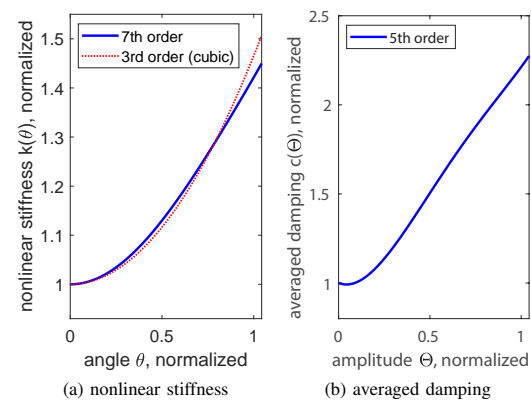


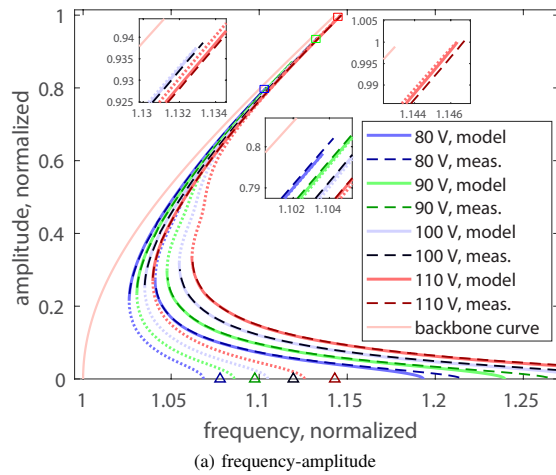
Fig. 5. Nonlinear stiffness function and averaged damping function from experimental identification. The stiffness identification using only linear and cubic terms is also drawn for comparison.

the response dynamics provided by the slow flow equations while eliminating deviations caused by imperfect knowledge of the real parameters.

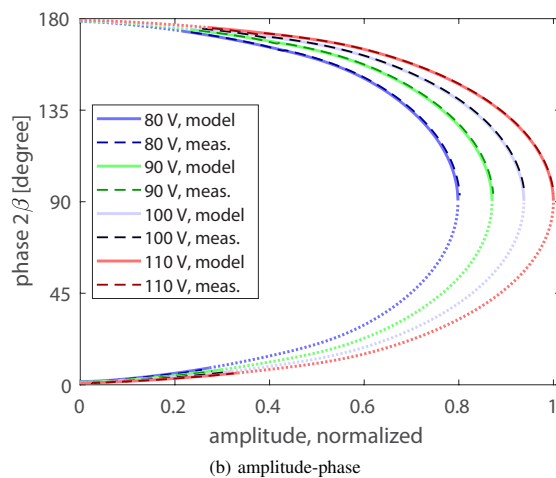
Here a model-based identification is newly employed by decoupling stiffness, capacitance, inertia, and damping parameters in independent measurements. The basic idea of decoupled measurements is presented in [14] and used for data-driven parameter identification for the SDOF model of (1). First of all, the nonlinear stiffness function is identified by the amplitude-frequency relation of the backbone curve, which is obtained by setting voltage U to zero in (28), i.e. the dimensionless Fourier coefficients $b(n)$ to zero. A 7th order polynomial function is used for a good approximation of the measurement data as in [14]. FEM simulation data of the restoring torque including the geometric nonlinearities of the leaf spring suspensions similarly require terms beyond the cubic for a satisfactory fit. By measuring the actuated decay, i.e. the ring-down oscillation with a DC voltage applied to the comb drives, the capacitance and angular derivative of the capacitance are obtained via the comb drive current with absolute dimension [14]. Using the amplitude-frequency relation of the actuated decay, the inertia of the mirror is obtained as a scaling parameter between normalized stiffening parameters and actuation influence in the primary frequencies. Finally, the averaged damping parameters are obtained from the measured stationary solutions by a square rooted sine input with a 120 V peak input voltage. Fig. 5 shows the normalized nonlinear stiffness function and the averaged damping function identified for the MEMS mirror. The amplitude and frequency values are normalized to the maximum amplitude with a 110 V input peak voltage and the linear mirror frequency, respectively.

A. Frequency Response

Frequency response is a set of stationary solutions of the parametrically driven resonant MEMS mirror. The frequency response is recorded by the beam trajectory measurements while sweeping up and down the actuation frequency in steps of 2 Hz. Due to a significantly hardening stiffness of the



(a) frequency-amplitude



(b) amplitude-phase

Fig. 6. Frequency response and amplitude-phase plot from the slow flow model (light solid and dotted lines) and measurements (dark dashed lines) for various peak input voltages. The stable and unstable solutions of the model are represented by the solid line and the dotted line, respectively. Dark colored triangles represent the measured lower bounds of the unstable region. The backbone curve is drawn by a bright pink line.

employed leaf spring suspension structure [14], [15], the used mirror can reach the maximum angle only by down-sweep first and up-sweep after the bifurcation. For convenience, the stable solutions at the low amplitude side and the high amplitude side are called bottom response curve and top response curve, respectively. The lower bound of the Mathieu instability region [34] can be identified by the first unstable point in an up sweep from the stable region, where no oscillation occurs, and vice versa in a down sweep.

Fig. 6a shows the frequency response of the slow flow model together with the measurement data. The peak input voltages of 80, 90, 100, and 110 V are chosen to verify the behavior with various input amplitudes. The two stationary solutions of (28) consist of unstable (solid lines) and stable branches (dotted lines), which stretch continuously from zero amplitude to the peak amplitudes where (28) has the equal

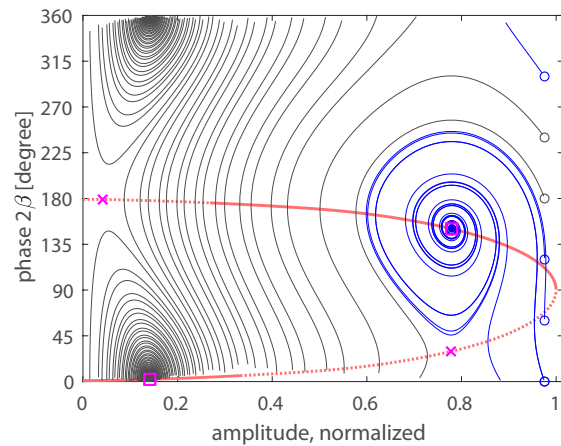


Fig. 7. Phase portrait and amplitude-phase plot (thick red lines) at the frequency of 1.1029 with 110 V peak input voltage. From initial conditions (circles) the slow flow dynamics lead to the stable equilibria (magenta squares) while the unstable equilibria are given by magenta x marks. The color of the trajectory represents its final steady state value, i.e. if it arrives at the solution of the top response curve (blue) or of the bottom response curve (dark gray).

roots. Since the unidirectional pulling torque by the out-of-plane comb drive adds only stiffness, both solutions lie on the high frequency side with respect to the backbone curve. In addition, both solutions get close to the backbone curve at high amplitudes due to the relatively high Q-factor, i.e. the energy injected by the comb drive per period is much smaller than the stored energy of the MEMS mirror. Especially, the model describes well the points of the bifurcation where the stability at the stationary solution changes. In general, the analytic solution of (28) shows a good match with the measurement data at large amplitudes. For amplitudes above 0.16, the normalized frequency errors are less than ± 0.0004 , which corresponds to less than ± 0.8 Hz peak errors for a 2 kHz linear mirror frequency. The maximum peak amplitude also shows a good agreement and the worst case error is 0.47 % in the 80 V peak input voltage case, which corresponds to 0.071° for a 15° amplitude.

For low amplitudes, the trends of the bottom response curves are similar even though the model does not show a good agreement anymore. From the model, the lower bound of the unstable region is represented by the zero crossing of the unstable solution that extends from the top response curve. The measured low bounds of the unstable solution have a large mismatch from the model. This mismatch is mainly due to the model error of (1), also shown by the ODE simulations in [14].

Fig. 6b illustrates the amplitude-phase plot of the model and measurements for various peak input voltages. The phase is calculated by zero crossing differences between the measured input signal from the function generator and the measured mirror angle, considering an identified delay between the input signal and the angle measurements. Because $\Omega_a = 2\sigma$, the double phase 2β of $\beta \in [0, \pi]$ is drawn since it is identical with $\beta \in [\pi, 2\pi]$. The model has a unique parabola-like shape, showing a good agreement with the measurements for all peak input voltages. The maximum amplitude is attained at

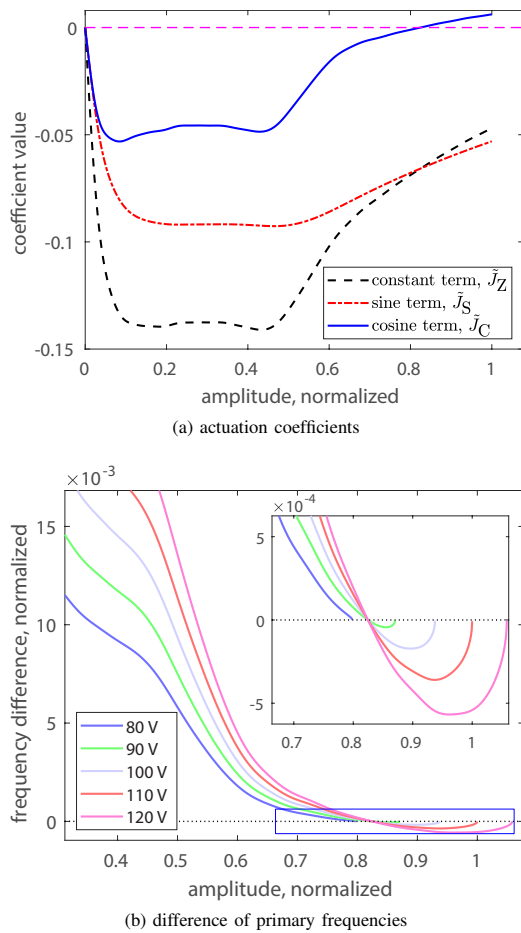


Fig. 8. Actuation parameters in the slow flow dynamics with a 110 V peak input voltage and difference between the two primary frequencies for various peak input voltages.

90° phase, which is expected by the synchronized excitation scheme [41].

Fig. 7 shows a phase portrait describing the global dynamics by (23) and (24). The initial conditions are chosen by an amplitude of 0.9755 and phases of $k\pi/6$, $k \in 0, 1, \dots, 5$ for the mirror frequency $\sigma = 1.1029$ with the peak input voltage of 110 V. The trajectories arrive at the two stable equilibria while the shape of contours allows to identify the unstable saddle points. Both stable and unstable solutions are located on the amplitude-phase plot in Fig 6b, and the location changes with frequency and peak input voltage. The size of the attraction for the stable equilibrium varies depending on the locations of the other solutions. For example, the attraction of the stable solution at the top response curve becomes smaller with increasing amplitude since the unstable saddle point approaches the stable solution. This explains why the synchronized excitation is difficult to attain in an open loop sweep.

The simulation also demonstrates the low computational effort by the proposed model. For 10,000 points of amplitudes,

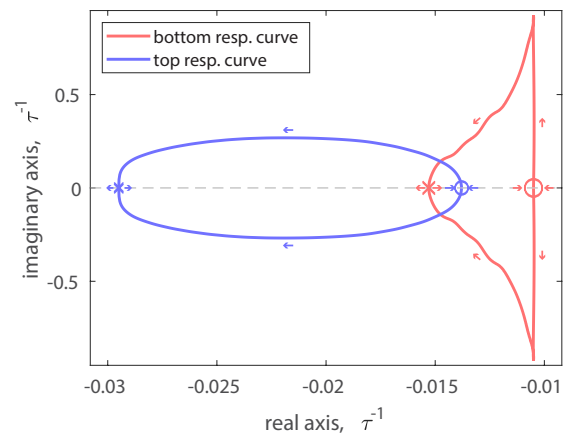


Fig. 9. Simulated evolution of the poles along the stable solutions of top response curve and bottom response curve with a 110 V peak input voltage. The lowest amplitude and highest amplitude are marked as circle and x mark, respectively, to show the direction of the pole movement by increasing amplitude (arrow direction).

the primary frequency and phase calculation by (28), (23), and (24) takes 0.57 s and the Jacobian matrix calculation of (30) takes 1.27 s by a Matlab 2018b script with a laptop PC (Intel Core-i7 8850H, 2.6 GHz). The simulation of the global dynamics in Fig. 7 takes 1.12 s average for a normalized time 5000 while the brute force simulation of (1) takes 1303.20 s. A direct comparison is not entirely meaningful since the information of the results is different, but it still illustrates the benefit of the computational efficiency of the proposed model.

B. Frequency Crossover between Solutions

The primary frequency of (28) features an interesting behavior of crossover between solutions. It is already visible in zoomed figures near $\sigma = 1.132$ in Fig. 6a that the frequency of the unstable solution is lower than the frequency of the stable solutions for a given amplitude. This is due to the sign change of the cosine actuation coefficients of \tilde{J}_C . Fig. 8a shows the actuation coefficients versus the amplitude. The cosine actuation coefficient shows a sign change at the amplitude of 0.824. This sign change results in a crossover of the frequency solution regardless of the actuation voltage, shown in Fig. 8b, except for the 80 V case, which cannot reach amplitudes higher than 0.824. This crossover is determined by the shape of the angular derivative of the comb drive capacitance, i.e. it can be controlled by the comb drive design.

C. Local Dynamics of Stable Equilibrium

Besides the global dynamics of the slow flow model, local dynamics near a stable equilibrium are also essential for understanding external vibration influences [25] and the design of the controls at a specific operational point [15]. For local dynamics, the poles of the Jacobian in (30) determine the main dynamic behavior. Fig. 9 describes the root locus of the complex valued poles of both top and bottom response curve.

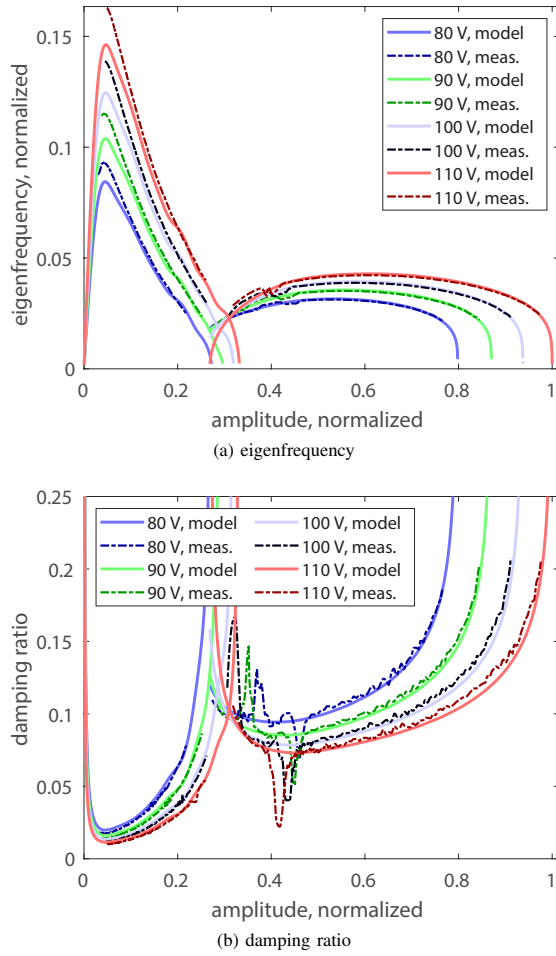


Fig. 10. Eigenfrequency and damping ratio of the Jacobian matrix and the measurements for various peak input voltages.

By the location of the poles, an eigenfrequency and damping ratio of the local dynamics are determined. The eigenfrequency and the damping ratio are measured by analyzing the transient response to a small change of the operational points, e.g. peak input voltages.

Fig. 10 depicts the eigenfrequency and the damping ratio of the local dynamics from the model and the measurements for various peak input voltages. The overall behavior especially at large amplitudes shows a good agreement. For the top response curve, the eigenfrequency and the damping ratio are about 0.03 and 0.12 and do not vary much for a large angular range while those of the bottom response curve change much with amplitudes. For each end of the response curve, the frequency reduces and the damping increases since the poles are closed to or on the real axis. As a trend, higher input peak voltages result in higher eigenfrequency and lower damping ratio. There is a large mismatch at amplitudes near 0.4 of the top response curve, which is due to mode coupling with the translational y-mode of the mirror.

These results prove that the proposed slow flow model with

a Fourier based torque approximation can accurately describe the mirror behavior at large amplitudes in characteristic properties, enabling the fast and accurate performance analysis of the MEMS mirror prior to the fabrication.

V. CONCLUSION

This paper proposes an accurate slow flow model of a parametrically driven MEMS mirror by a Fourier series based torque approximation. The Fourier series based torque model uses a discrete Fourier transform, allowing an accurate analytic approximation of the comb drive torque with a finite number of Fourier coefficients. By perturbation theory, the Fourier series based torque results in a slow flow model with Bessel functions, leading to a closed form of primary frequencies and the Jacobian matrix representing the stability and the local dynamics at the equilibrium points. The experimental results demonstrate the accuracy of the proposed model in the frequency response, showing less than 0.04 % frequency error for large amplitudes over 16 % of the maximum amplitude with a 110 V input peak voltage. The eigenfrequency and the damping ratio of the local dynamics also demonstrate a good agreement between the model and the measurement. This proposed model allows a fast and accurate design evaluation of the MEMS mirror prior to fabrication and a control design considering both global and local dynamics.

As future work, the slow flow model can be extended for a generalized input such as rectangular functions with varied duty cycle [10], [11], enabling a fast and accurate analysis of the most favorable and practical MEMS operation conditions. The local dynamics can be extended to include external vibration influence, which allows to evaluate the robustness of the mirror operation [25]. Similar to [42], the PLL control can be included for further analysis of the control design.

APPENDIX A PROOF OF THE LEMMA 1

For an integer order ν , the integral form of the Bessel function of the first kind can be expressed as

$$J_\nu(z) = \frac{1}{2\pi} \int_{-\pi}^{\pi} \cos(\nu w - z \sin w) dw,$$

since $\cos(\nu w - z \sin w)$ is an even function. Then each case can be calculated as follows.

1) Case $\int_0^{2\pi} \sin(\rho n A \cos \omega) \cos \omega d\omega$: By trigonometric identities,

$$\begin{aligned} & \int_0^{2\pi} \sin(\rho n A \cos \omega) \cos \omega d\omega \\ &= \frac{1}{2} \int_0^{2\pi} \sin(\omega + \rho n A \cos \omega) + \sin(-\omega + \rho n A \cos \omega) d\omega. \end{aligned}$$

By setting a new variable $\omega = w + \pi/2$, the integral interval is shifted as

$$\begin{aligned} & \frac{1}{2} \int_{-\pi}^{\pi} \cos(w - \rho n A \sin w) - \cos(-w - \rho n A \sin w) dw \\ &= \frac{1}{2} (2\pi J_1(\rho n A) - 2\pi J_{-1}(\rho n A)) = 2\pi J_1(\rho n A), \end{aligned}$$

by $J_{-\nu}(z) = (-1)^\nu J_\nu(z)$ for $\nu \in \mathbb{Z}$.

2) $\int_0^{2\pi} \sin(\rho n A \cos \omega) \sin \omega \, d\omega$: By similar way as in case 1),

$$\frac{1}{2} \int_{-\pi}^{\pi} \sin(w - \rho n A \sin w) + \sin(-w - \rho n A \sin w) \, dw = 0.$$

This is because the inside of the integral is an odd function.

3) $\int_0^{2\pi} \sin(\rho n A \cos \omega) \cos \omega \cos(2\omega - 2\beta) \, d\omega$: By trigonometric identities,

$$\begin{aligned} & \int_0^{2\pi} \sin(\rho n A \cos \omega) \cos \omega \cos(2\omega - 2\beta) \, d\omega \\ &= \frac{1}{4} \int_0^{2\pi} (\sin(3\omega + \rho n A \cos \omega) + \sin(-3\omega + \rho n A \cos \omega)) \, d\omega \cos 2\beta \\ &+ \frac{1}{4} \int_0^{2\pi} (\sin(\omega + \rho n A \cos \omega) + \sin(-\omega + \rho n A \cos \omega)) \, d\omega \cos 2\beta. \end{aligned}$$

The second part is given by $\pi J_1(\rho n A) \cos 2\beta$. By similar way in case 1), the first term with $\pm 3\omega$ is given as $-\pi J_3(\rho n A) \cos 2\beta$. This leads to

$$\begin{aligned} & \int_0^{2\pi} \sin(\rho n A \cos \omega) \cos \omega \cos(2\omega - 2\beta) \, d\omega \\ &= 2\pi \left(\frac{J_1(\rho n A) - J_3(\rho n A)}{2} \right) \cos 2\beta \\ &= 2\pi \left(J_1(\rho n A) - 2 \frac{J_2(\rho n A)}{\rho n A} \right) \cos 2\beta. \end{aligned}$$

The last line is given by the recurrence formulas, i.e. $J_{\nu+1}(z) = \frac{2\nu}{z} J_{\nu}(z) - J_{\nu-1}(z)$.

4) Case $\int_0^{2\pi} \sin(\rho n A \cos \omega) \sin \omega \cos(2\omega - 2\beta) \, d\omega$: By the similar way in case 3),

$$\begin{aligned} & \int_0^{2\pi} \sin(\rho n A \cos \omega) \sin \omega \cos(2\omega - 2\beta) \, d\omega \\ &= 2\pi \left(\frac{J_1(\rho n A) + J_3(\rho n A)}{2} \right) \sin 2\beta = 2\pi \left(2 \frac{J_2(\rho n A)}{\rho n A} \right) \sin 2\beta. \end{aligned}$$

APPENDIX B

DERIVATION OF THE SLOW FLOW MODEL

Before applying the solvability condition of (14), the derivative term is rewritten as

$$D_1 D_0 x_0 = -\frac{\partial A(T_1)}{\partial T_1} \sigma \sin \omega - \frac{\partial \beta(T_1)}{\partial T_1} \sigma A(T_1) \cos \omega.$$

Based on Lemma 1 and Corollary 2, the real part is reduced as

$$\begin{aligned} 0 &= \int_0^{2\pi} [2A\mu(A)\sigma \sin \omega \cos \omega + (\sigma^2 - 1) A \cos^2 \omega \\ &- K_3 A^3 \cos^4 \omega - K_5 A^5 \cos^6 \omega - K_7 A^7 \cos^8 \omega + (1 + \cos 2\sigma T_0)] \\ &\times \left(\frac{1}{2} a(0) + \sum_{n=1}^{N_L} a(n) \cos(\rho n A \cos \omega) + b(n) \sin(\rho n A \cos \omega) \right) \cos \omega \\ &+ 2 \frac{\partial A}{\partial T_1} \sigma \sin \omega \cos \omega + 2 \frac{\partial \beta}{\partial T_1} A \sigma \cos^2 \omega \, d\omega \\ &= \frac{2\pi(\sigma^2 - 1)A}{2} - 2\pi \frac{3K_3 A^3}{8} - 2\pi \frac{5K_5 A^5}{16} - 2\pi \frac{35K_7 A^7}{128} \\ &+ 2\pi \sigma A \frac{\partial \beta}{\partial T_1} + 2\pi \left(\sum_{n=1}^{N_L} b(n) J_1(\rho n A) \right) \\ &+ 2\pi \left(\sum_{n=1}^{N_L} b(n) \left(\frac{\rho n A J_1(\rho n A) - 2J_2(\rho n A)}{\rho n A} \right) \right) \cos 2\beta, \end{aligned}$$

and the imaginary part is then

$$\begin{aligned} 0 &= \int_0^{2\pi} [2A\mu(A)\sigma \sin^2 \omega + (\sigma^2 - 1) A \cos \omega \sin \omega \\ &- K_3 A^3 \cos^3 \omega \sin \omega - K_5 A^5 \cos^5 \omega \sin \omega - K_7 A^7 \cos^7 \omega \sin \omega \\ &+ \left(\frac{1}{2} a(0) + \sum_{n=1}^{N_L} a(n) \cos(\rho n A \cos \omega) + b(n) \sin(\rho n A \cos \omega) \right) \sin \omega \\ &\times (1 + \cos 2\sigma T_0) + 2 \frac{\partial A}{\partial T_1} \sigma \sin^2 \omega + 2 \frac{\partial \beta}{\partial T_1} A \sigma \cos \omega \sin \omega] \, d\omega \\ &= 2\pi \sigma \mu A + 2\pi \sigma \frac{\partial A}{\partial T_1} + 2\pi \left(\sum_{n=1}^{N_L} 2b(n) \left(\frac{J_2(\rho n A)}{\rho n A} \right) \right) \sin 2\beta. \end{aligned}$$

Equations in real and complex parts lead to two partial differential equations as

$$\frac{\partial A}{\partial T_1} = -A\mu(A) - \frac{1}{\sigma} \left(\sum_{n=1}^{N_L} 2b(n) \left(\frac{J_2(\rho n A)}{\rho n A} \right) \right) \sin 2\beta, \quad (38)$$

$$\begin{aligned} A \frac{\partial \beta}{\partial T_1} &= \frac{3K_3 A^3}{8\sigma} + \frac{5K_5 A^5}{16\sigma} + \frac{35K_7 A^7}{128\sigma} - \frac{(\sigma^2 - 1)A}{2\sigma} \\ &- \frac{1}{\sigma} \left(\sum_{n=1}^{N_L} b(n) J_1(\rho n A) \right) \\ &- \frac{1}{\sigma} \left(\sum_{n=1}^{N_L} b(n) \left(\frac{\rho n A J_1(\rho n A) - 2J_2(\rho n A)}{\rho n A} \right) \right) \cos 2\beta. \quad (39) \end{aligned}$$

By assuming $A > 0$ considering only the nontrivial solution and using the ordinary differential operator, (38) and (39) lead to (23) and (24). The primary frequency response is defined by the stationary solutions, i.e. $\frac{\partial A}{\partial T_1} = 0$ and $\frac{\partial \beta}{\partial T_1} = 0$, leading to (28).

ACKNOWLEDGMENT

The authors would like to thank to David Brunner and Richard Schroedter of ACIN in TU Wien for fruitful discussions.

REFERENCES

- [1] S. Hsu, T. Klose, C. Drabe, and H. Schenk, "Fabrication and characterization of a dynamically flat high resolution micro-scanner," *J. Opt. A: Pure Appl. Opt.*, vol. 10, no. 4, p. 044005, 2008.
- [2] S. T. S. Holmström, U. Baran, and H. Urey, "MEMS laser scanners: A review," *J. Microelectromech. Syst.*, vol. 23, no. 2, pp. 259–275, 2014.
- [3] A. Wolter, S.-T. Hsu, H. Schenk, and H. K. Lakner, "Applications and requirements for MEMS scanner mirrors," in *Proc. SPIE 5719*, Jan. 2005, pp. 64–76.
- [4] K. Ito, C. Niclass, I. Aoyagi, H. Matsubara, M. Soga, S. Kato, M. Maeda, and M. Kagami, "System design and performance characterization of a mems-based laser scanning time-of-flight sensor based on a 256x64-pixel single-photon imager," *IEEE Photonics J.*, vol. 5, p. 6800114, 2013.
- [5] U. Hofmann, M. Aikio, J. Janes, F. Senger, V. Stenchly, J. Hagge, H.-J. Quenzer, M. Weiss, T. v. Wantoch, C. Mallas, B. Wagner, and W. Benecke, "Resonant biaxial 7-mm MEMS mirror for omnidirectional scanning," *J. Micro/Nanolith. MEMS MOEMS*, vol. 13, no. 1, p. 011103, Dec. 2013.
- [6] T. Sandner, T. Grasshoff, M. Wildenhain, and H. Schenk, "Synchronized microscanner array for large aperture receiver optics of LIDAR systems," in *MOEMS and Miniaturized Systems IX*, vol. 7594, International Society for Optics and Photonics, Feb. 2010, p. 75940C.
- [7] T. Sandner, T. Grasshoff, M. Wildenhain, and M. Schwarzenberg, "Hybrid assembled MEMS scanner array with large aperture for fast scanning LIDAR systems," *tm - Technisches Messen*, vol. 86, no. 3, pp. 151–163, 2019.

- [8] H. W. Yoo, N. Druml, D. Brunner, C. Schwarzl, T. Thurner, M. Hennecke, and G. Schitter, "MEMS-based lidar for autonomous driving," *Elektrotechnik und Informationstechnik*, vol. 135, no. 6, pp. 408–418, 2018.
- [9] N. Druml, I. Maksymova, T. Thurner, D. van Lierop, M. Hennecke, and A. Foroutan, "1D MEMS Micro-Scanning LiDAR," in *Int. Conf. on Sensor Device Technologies and Appl.*, 2018.
- [10] W. Shahid, Z. Qiu, X. Duan, H. Li, T. D. Wang, and K. R. Oldham, "Modeling and Simulation of a Parametrically Resonant Micromirror With Duty-Cycled Excitation," *J. Microelectromech. Syst.*, 23(6): 1440–1453, 2014.
- [11] H. Li, P. Barnes, E. Harding, X. Duan, T. D. Wang, and K. R. Oldham, "Large-Displacement Vertical Electrostatic Microactuator Dynamics Using Duty-Cycled Softening/Stiffening Parametric Resonance," *J. Microelectromech. Syst.*, vol. 28, no. 3, pp. 351–361, 2019.
- [12] A. Frangi, A. Guerrieri, R. Carminati, and G. Mendicino, "Parametric Resonance in Electrostatically Actuated Micromirrors," *IEEE Trans. Ind. Electron.*, vol. 64, no. 2, pp. 1544–1551, Feb. 2017.
- [13] A. Frangi, A. Guerrieri, N. Boni, R. Carminati, M. Soldo, and G. Mendicino, "Mode Coupling and Parametric Resonance in Electrostatically Actuated Micromirrors," *IEEE Trans. on Ind. Electron.*, vol. 65, no. 7, pp. 5962–5969, Jul. 2018.
- [14] D. Brunner, H. W. Yoo, T. Thurner, and G. Schitter, "Data based modelling and identification of nonlinear SDOF MOEMS mirror," in *Proc. SPIE 10931*, 2019, p. 1093117.
- [15] D. Brunner, H. W. Yoo, and G. Schitter, "Linear modeling and control of comb-actuated resonant MEMS mirror with nonlinear dynamics," *IEEE Trans. Ind. Electron.*, vol. 67, no. -, p. In press, 2020.
- [16] C. Ataman and H. Urey, "Modeling and characterization of comb-actuated resonant microscanners," *J. Micromech. Microeng.*, vol. 16, no. 1, p. 9, 2006.
- [17] C. Ataman, H. Urey, and A. Wolter, "A Fourier transform spectrometer using resonant vertical comb actuators," *J. Micromech. Microeng.*, vol. 16, no. 12, pp. 2517–2523, 2006.
- [18] K. L. Turner, S. A. Miller, P. G. Hartwell, N. C. MacDonald, S. H. Strogatz, and S. G. Adams, "Five parametric resonances in a microelectromechanical system," *Nature*, vol. 396, no. 6707, pp. 149–152, Nov. 1998.
- [19] W. Zhang, R. Baskaran, and K. L. Turner, "Effect of cubic nonlinearity on auto-parametrically amplified resonant MEMS mass sensor," *Sensor. Actuat. A-Phys.*, vol. 102, no. 1, pp. 139–150, Dec. 2002.
- [20] W. Zhang and K. L. Turner, "Application of parametric resonance amplification in a single-crystal silicon micro-oscillator based mass sensor," *Sensor. Actuat. A-Phys.*, vol. 122, no. 1, pp. 23–30, Jul. 2005.
- [21] J. F. Rhoads, S. W. Shaw, K. L. Turner, J. Moehlis, B. E. DeMartini, and W. Zhang, "Generalized parametric resonance in electrostatically actuated microelectromechanical oscillators," *J. Sound Vib.*, vol. 296, no. 4, pp. 797–829, 2006.
- [22] T. Izawa, T. Sasaki, and K. Hane, "Scanning micro-mirror with an electrostatic spring for compensation of hard-spring nonlinearity," *Micromachines*, vol. 8, no. 8, p. 240, 2017.
- [23] K. B. Lee, "Non-contact electrostatic microactuator using slit structures: theory and a preliminary test," *J. Micromech. Microeng.*, vol. 17, no. 11, pp. 2186–2196, 2007.
- [24] Y. Linzon, B. Ilic, S. Lulinsky, and S. Krylov, "Efficient parametric excitation of silicon-on-insulator microcantilever beams by fringing electrostatic fields," *J. of Appl. Phys.*, vol. 113, no. 16, p. 163508, 2013.
- [25] H. W. Yoo and G. Schitter, "Complex valued state space model for weakly nonlinear Duffing oscillator with noncollocated external disturbance," in *21st IFAC World Congress*, Jul. 2020, p. in press.
- [26] E. Allgower and K. Georg, "Simplicial and Continuation Methods for Approximating Fixed Points and Solutions to Systems of Equations," *SIAM Rev.*, vol. 22, no. 1, pp. 28–85, 1980.
- [27] C. Padmanabhan and R. Singh, "Analysis of periodically excited nonlinear systems by a parametric continuation technique," *J. of Sound Vib.*, vol. 184, no. 1, pp. 35–58, Jul. 1995.
- [28] A. Frangi, A. Guerrieri, and N. Boni, "Accurate Simulation of Parametrically Excited Micromirrors via Direct Computation of the Electrostatic Stiffness," *Sensors*, vol. 17, no. 4, p. 779, 2017.
- [29] A. M. Elshurafa, K. Khirallah, H. H. Tawfik, A. Emira, A. K. S. A. Aziz, and S. M. Sedky, "Nonlinear dynamics of spring softening and hardening in folded-MEMS comb drive resonators," *J. Microelectromech. Syst.*, vol. 20, no. 4, pp. 943–958, 2011.
- [30] J. Han, L. Li, G. Jin, J. Feng, B. Li, H. Jia, and W. Ma, "Vibration Identification of Folded-MEMS Comb Drive Resonators," *Micromachines*, vol. 9, no. 8, p. 381, 2018.
- [31] A. H. Nayfeh, *Introduction to perturbation techniques*. Wiley, New York, 1981.
- [32] E. Esmailzadeh, D. Younesian, and H. Askari, *Analytical Methods in Nonlinear Oscillations*. Springer Netherlands, 2019.
- [33] R. Farrugia, B. Portelli, I. Grech, D. Camilleri, O. Casha, J. Micallef, and E. Gatt, "Air damping of high performance resonating micro-mirrors with angular vertical comb-drive actuators," *Microsyst. Technol.*, 2019.
- [34] I. Kovacic, R. Rand, and S. Mohamed Sah, "Mathieu's Equation and Its Generalizations: Overview of Stability Charts and Their Features," *Appl. Mech. Rev.*, vol. 70, no. 2, p. 020802, Mar. 2018.
- [35] J.-H. He, "Bookkeeping Parameter in Perturbation Methods," *Int. J. Nonlin. Sci. Num.*, vol. 2, no. 3, pp. 257–264, Sep. 2001.
- [36] K. Yagasaki, M. Sakata, and K. Kimura, "Dynamics of a weakly nonlinear system subjected to combined parametric and external excitation," *J. Appl. Mech.*, vol. 57, no. 1, pp. 209–217, 1990.
- [37] H. W. Yoo, D. Brunner, T. Thurner, and G. Schitter, "MEMS test bench and its uncertainty analysis for evaluation of MEMS mirrors," in *8th IFAC Symp. on Mechatronic Syst.*, Sep. 2019, pp. 49–54.
- [38] H. W. L. A. M. van Lierop, M. A. G. Suijlen, and M. J. van Os, "MEMS scanning micromirror," US Patent 9,588,337 B2, Mar., 2017.
- [39] J. Nee, R. Conant, R. Muller, and K. Lau, "Lightweight, optically flat micromirrors for fast beam steering," in *2000 IEEE/LEOS Int. Conf. on Opt. MEMS*, Aug. 2000, pp. 9–10.
- [40] H. W. L. A. M. van Lierop and M. A. G. Suijlen, "MEMS scanning micromirror," US Patent 9,910,269 B2, Mar., 2018.
- [41] D. Brunner, H. W. Yoo, and G. Schitter, "Digital asynchronous phase locked loop for precision control of MOEMS scanning mirror," in *8th IFAC Symp. on Mechatronic Syst.*, Sep. 2019, pp. 43–48.
- [42] X. Sun, R. Horowitz, and K. Komvopoulos, "Stability and Resolution Analysis of a Phase-Locked Loop Natural Frequency Tracking System for MEMS Fatigue Testing," *J. Dyn. Sys., Meas., Control*, vol. 124, no. 4, pp. 599–605, Dec. 2002.



optomechanics and adaptive optics for confocal microscopy. His main research interests are optical metrology, precision mechatronics systems, and biomedical imaging.



such as pressure sensors, accelerometers, and scanning mirror devices.



and lithography systems for semiconductor industry. He received the journal best paper award of IEEE/ASME Transactions on Mechatronics (2017), of the IFAC Mechatronics (2008-2010), of the Asian Journal of Control (2004-2005), and the 2013 IFAC Mechatronics Young Researcher Award. He served as an Associate Editor for IFAC Mechatronics, Control Engineering Practice, and for the IEEE Transactions on Mechatronics.

Han Woong Yoo is a postdoctoral researcher in Advanced Mechatronic Systems at the Automation and Control Institute (ACIN) of TU Wien. He received BS from Yonsei University and MS in Electrical Engineering from Seoul National University in 2007. Afterwards, he worked in Samsung Advanced Institute of Technology (SAIT) and Samsung Electronics co. LTD, semi-conductor business, for low power digital RF and algorithms for reliability of multi-level non-volatile memories. He received PhD in 2015 at Delft University of Technology about

Stephan Albert is Principal Engineer for MEMS Devices at Infineon Technologies AG in Neubiberg, Germany. He received an MA as Fulbright scholar from Stony Brook University (2007), a Diploma Degree from TU Munich (2010), and a PhD from TU Munich (2015) in physics. He has worked both experimentally in the fields of quantum optics, ultracold atoms, and magnetism as well as theoretically in the field of many-body physics. At Infineon he is responsible for the design, modeling, and the development of integration concepts for MEMS devices,

Georg Schitter is Professor for Advanced Mechatronic Systems at the Automation and Control Institute (ACIN) of TU Wien. He received an MSc in Electrical Engineering from TU Graz, Austria (2000) and an MSc and PhD degree from ETH Zurich, Switzerland (2004). His primary research interests are on high-performance mechatronic systems, particularly for applications in the high-tech industry, scientific instrumentation, and mechatronic imaging systems, such as AFM, scanning laser and LIDAR systems, telescope systems, adaptive optics,